Applied Catalysis A, General 595 (2020) 117507

Contents lists available at ScienceDirect

Applied Catalysis A, General

journal homepage: www.elsevier.com/locate/apcata

A novel microreaction strategy to fabricate superior hybrid zirconium and zinc oxides for methanol synthesis from CO_2

Xiuxiu Wang[a,b,c,1], Yizhou Wang[a,b,c,1], Chunliang Yang[a,b,c], Yun Yi[a,b,c], Xiaodan Wang[b,c], Fei Liu[a,b,c,*], Jianxin Cao[a,b,c,*], Hongyan Pan[a,b,c]

[a] School of Chemistry and Chemical Engineering, Guizhou University, Guiyang, Guizhou, 550025, PR China
[b] Key Laboratory of Green Chemical and Clean Energy Technology, Guizhou University, Guiyang, Guizhou, 550025, PR China
[c] Engineering Research Center of Efficient Utilization for Industrial Waste, Guizhou University, Guiyang, Guizhou 550025, PR China

ARTICLE INFO

Keywords:
Microreaction synthesis
ZnO/t-ZrO_2 hybrid oxide
Synergetic interaction
Oxygen vacancy defect
CO_2 hydrogenation

ABSTRACT

The synergetic interaction of solid solutions plays important roles in the reaction efficiency of CO_2 hydrogenation, which is used to produce methanol. The effects of material mixing, impregnation, traditional coprecipitation, and microreaction synthesis on the structural and catalytic properties of ZnO/t-ZrO_2 hybrid oxides were investigated. Although the impregnation effect caused a certain electronic structural modulation at the Zn/Zr interface, the pore structure blocking effect and low number of oxygen vacancy defects leaded to a low catalytic reaction efficiency. The solid solution structure enhanced the Zn/Zr interfacial interaction and increased the electron binding energy. More importantly, many oxygen vacancy defects were formed, which promoted CO_2 activation. However, the solid solution structure was more affected by the preparation method. The solid solution formed from the microreaction exhibited excellent catalytic activity, thermal stability and regeneration performance due to a more uniform solid solution structure and abundant oxygen vacancy defects. The CO_2 conversion rate, methanol selectivity, and methanol space-time yield (STY) under the conditions of H_2/CO_2 = 3:1, 320 °C, 3 MPa, GHSV = 12,000 ml g^{-1} h^{-1} reached 9.2 %, 93.1 %, and 0.35 g_{MeOH} $h^{-1}g_{cat}{}^{-1}$, respectively.

1. Introduction

Large amounts of CO_2 have been released into the atmosphere, causing increasing environmental and ecological problems and resource utilization [1]. Open-bond reduction and constant-valence compounding are the two primary pathways for the chemical conversion of CO_2 to carbon-containing products [2]. The CO_2 molecule is relatively stable, and a relatively high energy barrier must be overcome in order to activate it. High-energy hydrogen, derived from sustainable energy resources including solar energy and wind energy [3,4], can be used to reduce CO_2 to methanol, which not only recycles C and reduces CO_2 emissions, but also alleviates the dependence of methanol production on non-renewable resources, such as coal and natural gas.

Many industrial catalysts for methanol synthesis via CO_2 conversion have been developed, such as Cu-based [5–8] (Cu/ZnO/Al_2O_3, Cu/ZrO_2, Cu/ZnO, Cu/ZnO/ZrO_2) and noble metal Pd- and Pt-based catalysts ($GaPd_2/SiO_2$, PtCo/CeO_2) [9,10]. However, these catalysts are only suitable for low-temperature reactions in the range of 220 − 270 °C. As the reaction temperature increases, the CO_2 conversion rate increases, but the methanol selectivity and thermal stability of the catalyst decrease because the metallic active components in the catalysts are prone to sinter and rapidly deactivate. In recent years, with the successful development of solid solution structures, such as ZnO-ZrO_2 and InO-ZrO_2 oxides [11,12], thermally stable CO_2 conversion has been achieved in catalytic systems operated above 300 °C. It is generally believed that CO_2 is activated by oxygen vacancies after being adsorbed by basic sites. H_2 undergoes a hydrogen overflow effect due to the surface charge of the metal atom and migrates to CO_2* to form a HCOO* reactive intermediate. Then, continuous hydrogenation protonates H_3CO* to form methanol [13,14]. It was found that the special interaction significantly impact the catalytic performance of CO_2 hydrogenation to methanol. The formation of many oxygen vacancy defects in the structure plays a crucial role in the catalytic adsorption conversion of CO_2 and the formation of HCOO* active intermediates [15–22].

Therefore, it is necessary to further explore the influence of

* Corresponding authors at: School of Chemistry and Chemical Engineering, Guizhou University, Guiyang, Guizhou, 550025, PR China.
E-mail addresses: ce.feiliu@gzu.edu.cn (F. Liu), jxcao@gzu.edu.cn (J. Cao).
[1] These authors contributed equally to this work and should be considered co-first authors.

https://doi.org/10.1016/j.apcata.2020.117507
Received 5 January 2020; Received in revised form 1 March 2020; Accepted 2 March 2020
Available online 02 March 2020
0926-860X/

interfacial interaction of Zn/Zr on the hydrogenation of CO_2 to methanol, and establish structure-activity relationships of complex oxides. In this work, ZnO/t-ZrO_2 composite oxides were prepared by a microreaction synthesis method in a membrane separation microreactor. Such a design takes advantage of the unique high mixing efficiency and high mass and heat transfer characteristics of microreaction synthetic technology. The effects of compound mixing, impregnation, traditional coprecipitation, and microreaction synthesis on the structural and catalytic properties of composite oxides were investigated and compared. The determination of the most synergetic interaction for CO_2 hydrogenation to methanol are expected to improve the catalytic reaction efficiency of the process and enable the industrialization of the reaction process.

2. Experimental

2.1. Methods

2.1.1. Microreaction synthesis

Zinc-zirconium hybrid oxide was prepared by a microreaction synthesis method. A microreactor device was used, and the technical route is shown in Fig. 1. The dimensions of the microreactor were 6 cm × 5.5 cm × 3 cm, and the diameter of microsieve tunnel was 0.22 nm. The microreactor consisted of two stainless-steel plates and a stainless-steel microfiltration membrane. The microreactor was divided into a dispersed phase channel and a continuous phase channel by the microsieve. $Zn(NO_3)_2{\cdot}6H_2O$ (0.73 g) and $Zr(NO_3)_4{\cdot}5H_2O$ (6.34 g) in a Zn/Zr molar ratio of 1:6 were dissolved in deionized (DI) water to prepare a 0.3 mol/L mixture as the dispersed phase. $(NH_4)_2CO_3$ (3.07 g) was dissolved in DI water to make a 0.1 mol/L solution as the continuous phase. The microreaction synthesis was carried out at 80 °C, and the above-mentioned dispersed phase and continuous phase were injected into the microreactor by a parallel flow pump at a flow rate of 20 mL/min. The precursor of the reaction product was aged at 80 °C for 2 h, cooled to room temperature, successively washed three times with DI water and ethanol, dried at 80 °C for 10 h, and then calcined at 500 °C for 3 h to obtain the zinc-zirconium hybrid oxide, which was labelled as ZnO/t- ZrO_2-MR.

To prepare the sole t-ZrO_2, the dispersed phase in the microreaction preparation process was changed to $Zr(NO_3)_4{\cdot}5H_2O$ solution.

To prepare the sole ZnO, the dispersed phase in the microreaction preparation process was changed to $Zn(NO_3)_2{\cdot}6H_2O$ solution.

2.1.2. Traditional liquid phase coprecipitation method

Zinc-zirconium hybrid oxide was prepared by a liquid phase coprecipitation method. Using a Zn/Zr molar ratio of 1:6, 0.73 g Zn $(NO_3)_2{\cdot}6H_2O$ and 6.34 g $Zr(NO_3)_4{\cdot}5H_2O$ were dissolved in DI water to prepare a 0.3 mol/L mixed solution. $(NH_4)_2CO_3$ (3.07 g) was dissolved in DI water to prepare a 0.1 mol/L precipitant solution. The precipitating agent was added dropwise to the zinc-zirconium mixed solution at a rate of 3 mL/min^{-1}, and the reaction was carried out with magnetic stirring at 80 °C for 2 h. The product precursor was aged at 80 °C for 2 h, and cooled to room temperature. It was successively washed three times with water and ethanol, dried at 80 °C for 10 h, and calcined at 500 °C for 3 h to obtain the zinc-zirconium hybrid oxide, which was labelled ZnO/t-ZrO_2-CP.

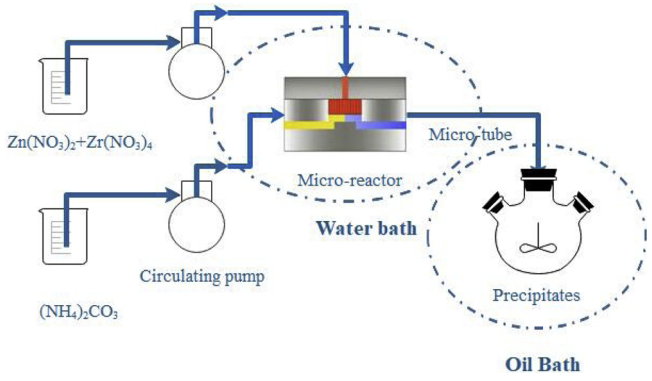

Fig. 1. Experimental microreactor device for preparing ZnO/t-ZrO_2-MR nanoparticles.

2.1.3. Incipient wetness impregnation

Zinc-zirconium hybrid oxide was prepared by an incipient wetness impregnation method. A $Zn(NO_3)_2{\cdot}6H_2O$ solution with concentration of 0.6 mol/L was prepared using a 1:6 M ratio of Zn/Zr. Equal volumes of the prepared $Zn(NO_3)_2{\cdot}6H_2O$ solution and 200 mesh t-ZrO_2 with water absorption of 0.5 g/mL were impregnated at room temperature for 12 h, dried at 80 °C for 10 h, and calcined at 500 °C for 3 h to obtain the zinc-zirconium hybrid oxide, which was labelled ZnO/t-ZrO_2-IM.

2.1.4. Physical blending method

Using a 1:6 M ratio of Zn/Zr, 0.1 g of ZnO and 0.9 g of t-ZrO_2 were weighed and thoroughly mixed to obtain a physically blended sample, which was labelled ZnO/t-ZrO_2-PB.

2.2. Catalyst characterization

The crystal phase composition and lattice structure of the samples were analyzed using an X'Pert Powder X-ray polycrystal diffractometer (PANalytical, Netherlands) with CuKα as the radiation source, a tube voltage of 40 kV, a tube current of 40 mA, a scanning range of 2θ = 5 - 90°, a scanning speed of 5°·min^{-1}, and a step size of 0.02°. The valence, binding energy, surface element content, and oxygen vacancies of samples were analyzed by a K-Alpha Plus X-ray photoelectron spectrometer (Thermo Fisher, USA), with Al-Kα radiation (1486.6 eV) and a power of 150 W. The sample's element content was analyzed by Malvern Panalytical Company's Zetium multi-function X-ray fluorescence spectrometer with a power of 4 kW. The microstructure of samples was analyzed by an IGMA + X-Max 20 scanning electron microscope (ZEISS, Germany) with an accelerating voltage of 30 kV. The microstructure of the sample was analyzed and characterized by a FeiTitan 80 200 kV field emission transmission electron microscope with a test voltage of 200 kV. The surface acidity and alkalinity of samples were analyzed by an AutoChem II2920 automatic temperature programmed chemical adsorption instrument (Micromeritics, U.S.A.). The N_2 flow rate was 40 ml·min^{-1}, the filling amount was 80 mg, and the desorption heating rate was 15 °C min^{-1}. H_2-TPR: the redox performance of samples was analyzed and characterized by an AutoChem II2920 automatic temperature-programmed chemical adsorption instrument (Micromeritics, U.S.A.) with the following parameters: Ar purging at a flow rate of 30 ml/min, heating at a rate of 10 °C/min to 150 °C after preheating for a 30 min, cooling to 50 °C, purging for 60 min with 10 % H_2 and 90 % Ar atmosphere, heating to 700 °C at a rate of 5 °C/min. The TPR signal data was recorded. O_2-TPO: nitrogen atmosphere was purged at a flow rate of 30 ml/min, and a heating rate of 10 °C/min to 200 °C for a 30 min preheating, cooled to 50 °C in a 2% O_2 / 98 % He atmosphere, purged until the baseline was stable, heated to 800 °C at a rate of 10 °C/min, and then the TPO signal data was recorded. The specific surface area and pore structure parameters of samples were analyzed by an ASAP 2020(M) automatic surface area micropore analyzer (Micromeritics, U.S.A.). Samples were degassed at 250 °C for 3 h, and the nitrogen adsorption/desorption temperature was 77 K. The specific surface areas of samples were calculated using the BET equation, and the pore size distributions of samples were calculated using DFT theory, P/P_0 = 0.995. Oxygen vacancies in samples were also analyzed and characterized using a Shimadzu UV-3600 plus UV–vis-NIR spectrophotometer. The test wavelength range was 200 nm–800 nm.

2.3. Catalyst evaluation

Catalyst performance was evaluated in a pressurized fixed bed reactor. Catalyst (1.0 g) was packed in the constant temperature zone of a fixed-bed stainless steel reaction tube (the upper and lower parts were filled with quartz wool). After leak detection was performed, reaction gases CO_2 and H_2 were fed into the reactor, with $V(H_2)$: $V(CO_2)$: $V(N_2)$ = 72:24:4, a reaction pressure of 3 MPa, 320 °C, and a gas hourly space velocity GHSV of 12,000 ml g^{-1} h^{-1}. CH_4 and CO_2 in the reaction product were measured using a GC9560 gas chromatograph equipped with a TCD detector. The CH_4 and CH_3OH in the reaction product were measured by a GC9560 gas chromatograph using an FID detector.

The normalization method was used to calculate the CO_2 conversion, methanol space-time yield (STY), selectivity of methanol, carbon monoxide, methane and dimethyl ether [11]. All data was recorded after a 3 h reaction time.

$$X(CO_2) = \frac{f_{CO}A_{CO} + i(f_{CH_4}A_{CH_4} + f_{CH_3OH}A_{CH_3OH} + 2f_{CH_3OCH_3}A_{CH_3OCH_3})}{f_{CO_2}A_{CO_2} + f_{CO}A_{CO} + i(f_{CH_4}A_{CH_4} + f_{CH_3OH}A_{CH_3OH} + 2f_{CH_3OCH_3}A_{CH_3OCH_3})}$$

$$S(CH_3OH) = \frac{i * f_{CH_3OH}A_{CH_3OH}}{f_{CO}A_{CO} + i(f_{CH_4}A_{CH_4} + f_{CH_3OH}A_{CH_3OH} + 2f_{CH_3OCH_3}A_{CH_3OCH_3})}$$

$$S(CO) = \frac{i * f_{CO}A_{CO}}{f_{CO}A_{CO} + i(f_{CH_4}A_{CH_4} + f_{CH_3OH}A_{CH_3OH} + 2f_{CH_3OCH_3}A_{CH_3OCH_3})}$$

$$S(CH_4) = \frac{i * f_{CH_4}A_{CH_4}}{f_{CO}A_{CO} + i(f_{CH_4}A_{CH_4} + f_{CH_3OH}A_{CH_3OH} + 2f_{CH_3OCH_3}A_{CH_3OCH_3})}$$

$$S\left(CH_3OCH_3\right) = \frac{i * 2f_{CH_3OCH_3}A_{CH_3OCH_3}}{f_{CO}A_{CO} + i(f_{CH_4}A_{CH_4} + f_{CH_3OH}A_{CH_3OH} + 2f_{CH_3OCH_3}A_{CH_3OCH_3})}$$

$$i = \frac{f_{CH_4-TCD}A_{CH_4-TCD}}{f_{CH_4-FID}A_{CH_4-FID}}$$

$$STY = \frac{GHSV}{22.4} \times V\%(CO_2) \times X(CO_2) \times S\left(CH_3OH\right) \times M\left(CH_3OH\right)$$

2.4. Hybrid oxide structure properties

The XRD patterns and corresponding lattice stress curves of zinc-zirconium hybrid oxides prepared by different methods are shown in Fig. 2. It can be seen from Fig. 2a that the mixed sample consisted of two phases of ZnO and ZrO_2. ZnO was a hexagonal wurtzite (corresponding to PDF card number 76-0704), and ZrO_2 was a tetragonal phase (corresponding to PDF card number 79–1769). The two-phase diffraction peak of the physically mixed sample was consistent with the standard cards, indicating that the two phases were only physically mixed, and no special chemical interaction occurred. Compared with the physically mixed sample, the intensities of the ZnO diffraction peaks of the impregnated sample were attenuated, indicating that the ZnO component in the impregnated sample was highly dispersed in the zirconia. The diffraction peaks generally shifted to lower angles, indicating that there might be an interaction between these two components in the impregnated sample. Interestingly, the diffraction peaks of the ZnO crystal phase were not observed in the samples prepared by the conventional coprecipitation and microreaction synthesis methods. The diffraction angles corresponding to the (101) and (110) crystal planes of ZrO_2 crystals shifted to higher angles, indicating that the prepared samples had unique solid solution structures. This was mainly due to the Jahn-Teller elongation effect [23]. When ZnO component was dissolved into ZrO_2, the Zr-O bond was shortened, and the corresponding interplanar spacing was reduced, resulting in an increase in the diffraction angle. Furthermore, the peak shifts of the (101) and (110) planes of the ZrO_2 crystals in the microreaction samples were more pronounced than those in the conventional co-precipitated samples. This indicated to some extent that the ZnO/t-ZrO_2-MR samples formed more solid solution defects. This was also confirmed by the UV–vis near-infrared absorption spectroscopy results (Fig. S1). The absorption peaks in the spectra of ZnO/t-ZrO_2-MR samples were significantly red shifted. The red shift was mainly caused by the smaller Zn^{2+} replacing the larger Zr^{4+}, which decreased the band gap, further indicating the existence of many solid solution defects [24,25]. Therefore, the microreaction synthetic route provided strong mixing efficiency and high mass transfer with its unique microchannels. Combined with the constant pH reaction system during the process, this provided a relatively uniform and rapid path for the formation of ZnO component in the initial precipitated product.

Fig. 2b shows the lattice stress curves of different samples calculated by the Williamson-Hall equation [26,27]. The slope of the curve represents the strength of the interaction between the zinc and zirconium components. The figure shows that the slope of the curve formed by the impregnated ZnO/t-ZrO_2-IM sample increased compared with the mixed ZnO/t-ZrO_2-PB sample, although a larger slope was observed in the solid solution structure sample. Compared to the traditional co-precipitation sample ZnO/t-ZrO_2-CP, the slope of the curve of ZnO/t-ZrO_2-MR prepared by microreaction synthesis was the largest, indicating that the zinc-zirconium composition of the sample had the strongest interaction and many defects. This can also be further confirmed by X-ray photoelectron spectroscopy of different catalysts

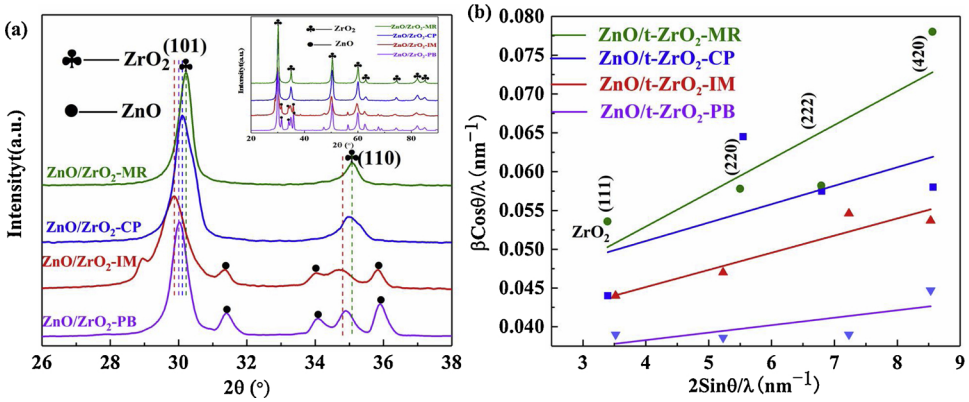

Fig. 2. Crystalline structure of ZnO/t-ZrO_2-MR, ZnO/t-ZrO_2-CP, ZnO/t-ZrO_2-IM and ZnO/t-ZrO_2-PB catalysts. (a) XRD patterns of various catalysts. (b) Lattice stress curves of various catalysts.

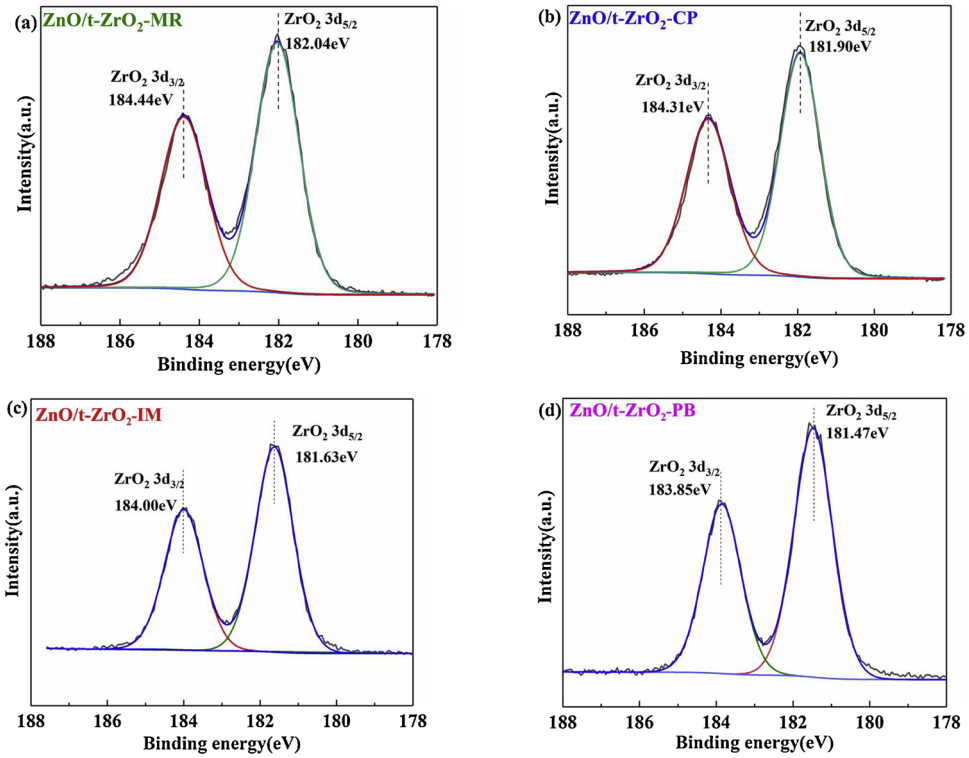

Fig. 3. XPS spectra of ZnO/t-ZrO_2-MR, ZnO/t-ZrO_2-CP, ZnO/t-ZrO_2-IM and ZnO/t-ZrO_2-PB catalysts.

(Fig. 3). The binding energies of the solid solution samples prepared by the microreaction synthesis and traditional coprecipitation methods were larger than those of the samples prepared by the impregnation method. This indicates that Zn^{2+} in the solid solution more strongly interacted with Zr^{4+}. In the solid solution samples, further comparison revealed a larger Zn/Zr binding energy in the ZnO/t-ZrO_2-MR sample. The outermost electrons of Zr shifted toward Zn during the complex impregnation and solid solution in the Zn/Zr composite, which decreased the density of the outermost electron cloud of Zr and increased its electron binding energy. However, ZnO component can undergo isomorphous substitution in the ZrO_2 precursor during solid solution processing, and the interaction of the two-phase elements was further enhanced. Comparing the Zn/Zr ratio from the XPS surface and XRF bulk phase spectra of different catalysts (Table S1), the increase in the electron binding energy of the solid solution prepared by microreaction synthesis was mainly attributed to better solid solution dispersibility of ZnO component. The transmission electron microscopy (TEM) images and scanning element distribution by scanning electron microscopy (SEM) test of traditional coprecipitation and microreaction synthesis samples are shown in Fig. 4. From the TEM images and particle size distributions, ZnO/t-ZrO_2-MR had smaller grain size and more centralized distribution compared with ZnO/t-ZrO_2-CP. The high-resolution lattice fringe TEM patterns and SEM element distribution of the samples further indicated that the ZnO component of ZnO/t-ZrO_2-MR presented a better dispersibility, and the solid solution structure of the sample was more uniform.

The O1s XPS spectra of different samples are shown in Fig. 5. The peak at a binding energy of 529 − 530 eV was attributed to lattice oxygen (O_{Latt}), and the binding energy at 530 − 532 eV was attributed to defective oxide or surface oxygen (O_{Sur}) [28]. Combined with the O_{Sur} /(O_{Latt} + O_{Sur}) data in Table 1, O_{Sur} /(O_{Latt} + O_{Sur}) in ZnO/t-ZrO_2-MR was 49 %, which was significantly higher than other samples, indicating that the sample had more oxygen vacancy defects. O_2-TPO analysis of different solid solution samples are shown in Fig. 6. The desorption peak from 50 − 200 °C was attributed to α-oxygen, which was mainly oxygen adsorbed on surface oxygen vacancies. The desorption peak from 300 − 780 °C was attributed to β-oxygen, which was mainly lattice oxygen [29]. Compared with ZnO/t-ZrO_2-CP, the β-oxygen desorption peak of ZnO/t-ZrO_2-MR shifted to a lower temperature and the desorption was larger, indicating that the solid solution had a better desorption capacity and more oxygen vacancies. The H_2-TPR analysis of different samples (Fig. S2) showed that the reduction temperature of ZnO/t-ZrO_2-MR shifted to lower temperatures, which further confirmed that the solid solution had a strong ability to generate, migrate, and transform active oxygen.

Different preparation methods greatly influenced the interaction of the Zn/Zr composite interface. The physically-mixed ZnO/t-ZrO_2-PB was only a simple physical mixture, and no special chemical interaction existed. The impregnated sample ZnO/t-ZrO_2-IM prepared by Zn impregnation on t-ZrO_2 as the carrier formed a particular interaction, which caused a change in the electronic structure properties of the sample. A larger electronic structure modulation was observed in the solid solution sample, and the special synergetic interaction formed changed the Zn/Zr electron binding energy, and generated oxygen vacancy defects. Compared with ZnO/t-ZrO_2-CP, ZnO/t-ZrO_2-MR had a more uniform ZnO component distribution, which resulted in the largest structural property modulation range and the most oxygen vacancy defects formed. This can also be confirmed from the CO_2 adsorption characteristics data of different solid solution samples, as shown in Fig. 7. It is not difficult to see that ZnO/t-ZrO_2-MR showed a larger CO_2 adsorption capacity and exhibited a potential CO_2 activation ability.

Although all composite samples prepared by different preparation methods were mesoporous, ZnO/t-ZrO_2-MR had the largest specific surface area of 38.65 m^2/g and a pore volume of 0.084 m^3/g (Fig. S3 and Table S2). This was related to the excellent mixing efficiency and mass and heat transfer characteristics of the microreaction process. The constant pH during the reaction promoted the effective collision of colloidal particles and easily controlled nucleation. Localized mixing tended to exist in the traditional coprecipitation method, and the unstable pH of the reaction system during the process caused particle agglomeration, which was not conducive to nucleation control.

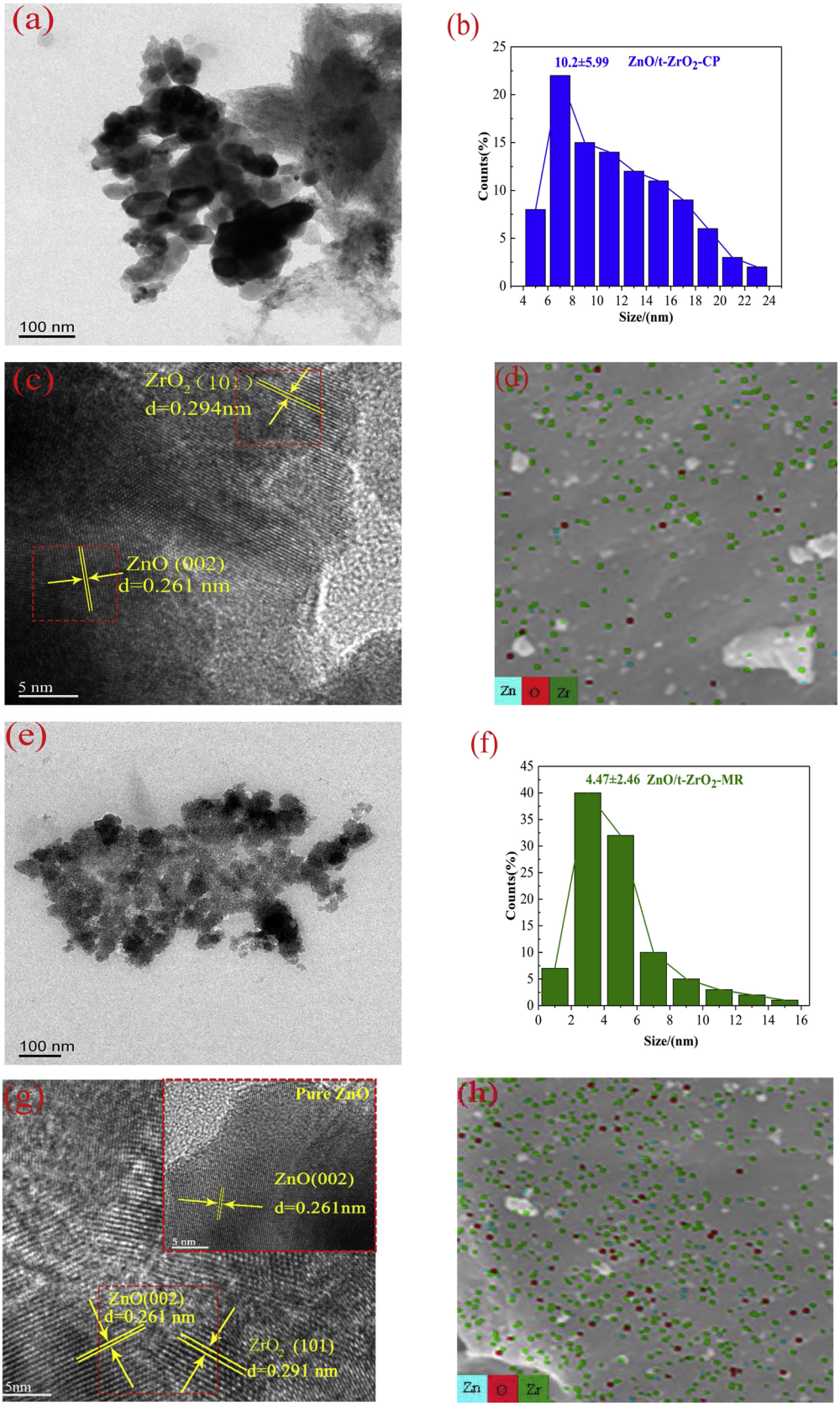

Fig. 4. TEM and scanning element distribution (SEM) images of ZnO/t-ZrO_2 binary. (a, e) TEM images of ZnO/t-ZrO_2-CP and ZnO/t-ZrO_2-MR. (c, g) HRTEM images of ZnO/t-ZrO_2-CP and ZnO/t-ZrO_2-MR. (b, f) Particle size distribution of ZnO/t-ZrO_2-CP and ZnO/t-ZrO_2-MR. (d, h) Scanning element distribution of ZnO/t-ZrO_2-CP and ZnO/t-ZrO_2-MR.

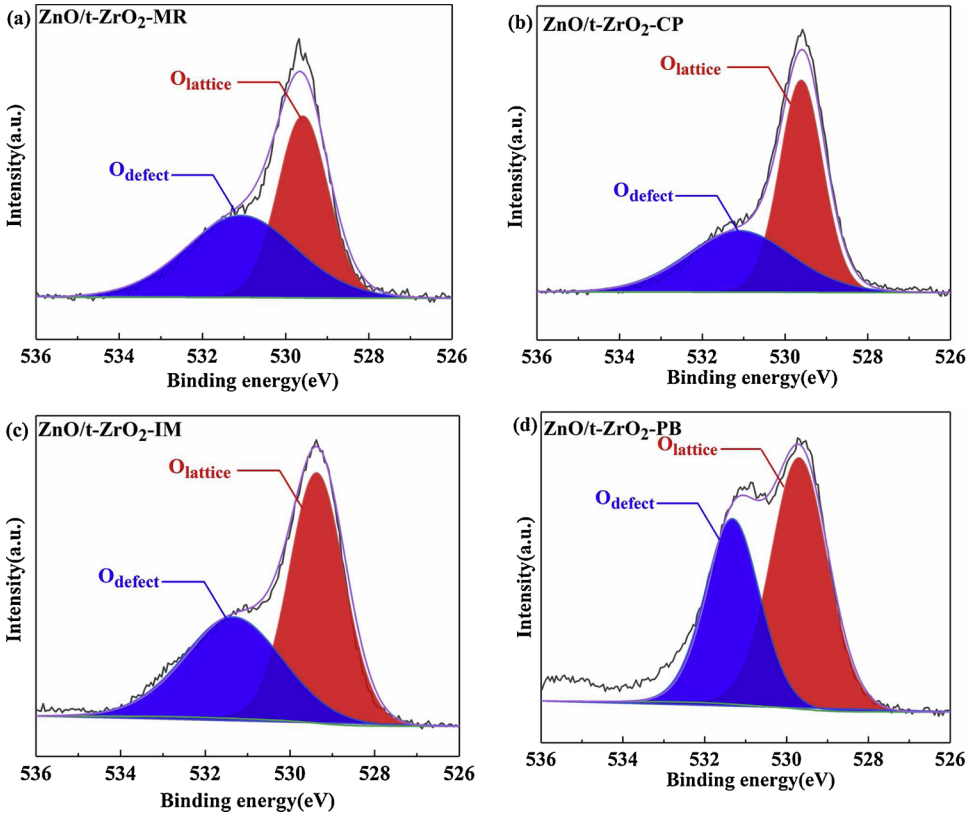

Fig. 5. XPS spectra of O1s in various catalysts.

Table 1
XPS results of ZnO/t-ZrO_2-MR, ZnO/t-ZrO_2-CP, ZnO/t-ZrO_2-IM and ZnO/t-ZrO_2-PB catalysts.

Catalyst	Binding energy (eV)		O_{Sur} /(O_{Latt} + O_{Sur}) (100%)
	O_{Latt}	O_{Sur}	
ZnO/t-ZrO_2-MR	529.54	531.03	49
ZnO/t-ZrO_2-CP	529.56	531.07	43
ZnO/t-ZrO_2-IM	529.32	531.29	39
ZnO/t-ZrO_2-PB	529.64	531.27	37

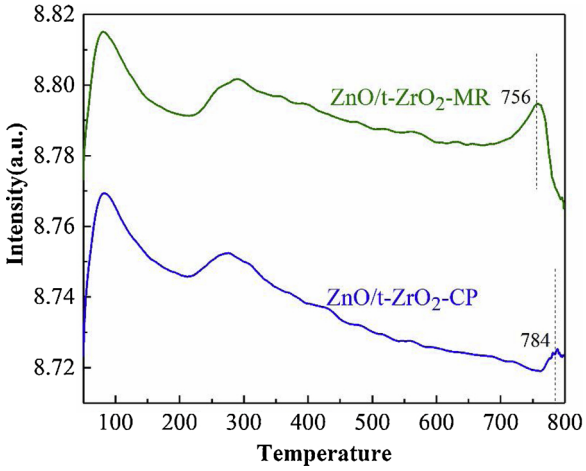

Fig. 6. O_2-TPO profiles of ZnO/t-ZrO_2-MR and ZnO/t-ZrO_2-CP.

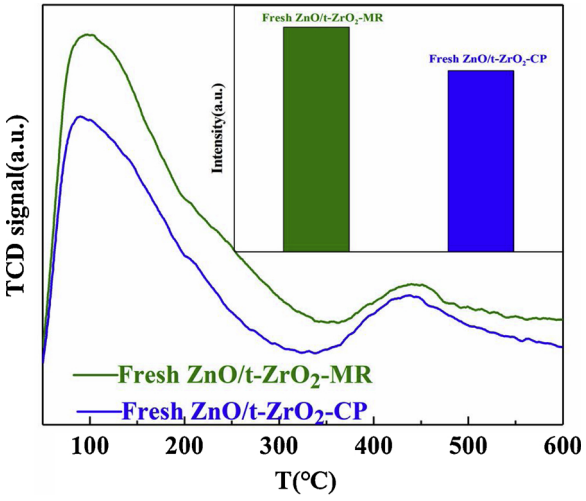

Fig. 7. CO_2-TPD profiles of various catalysts Fresh ZnO/t-ZrO_2-MR and ZnO/t-ZrO_2-CP.

3. Catalytic performance

In order to understand the relationship between composite sample structural properties and the CO_2 hydrogenation to methanol, the CO_2 conversion rate, methanol selectivity, and methanol space-time yield (STY) of different ZnO/t-ZrO_2 hybrid samples were investigated under the conditions of H_2/CO_2 = 3:1, 320 °C, 3 MPa, GHSV = 12,000 ml g^{-1} h^{-1}, and the results are shown in Fig.8. Carbon monoxide and dimethyl ether were examined as the main by-products apart from methane (Table S3). The figure clearly shows that ZnO/t-ZrO_2-IM had the worst catalytic performance, with the lowest CO_2 conversion rate, methanol selectivity, and methanol STY. From the above analysis,

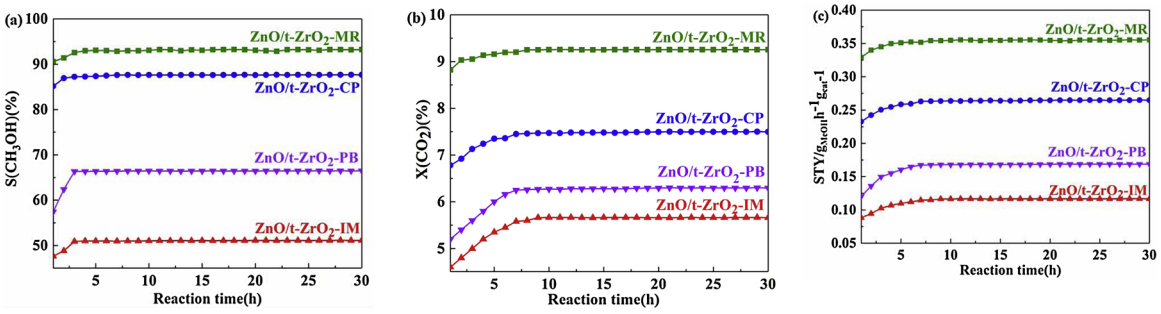

Fig. 8. Catalytic performance of ZnO/t-ZrO_2-MR, ZnO/t-ZrO_2-CP, ZnO/t-ZrO_2-IM and ZnO/t-ZrO_2-PB catalysts.

compared to the physically mixed sample, the Zn/Zr interfacial interaction formed by the impregnation of ZnO component on the surface of t-ZrO_2 changed the electronic properties of the sample. However, it can be seen from the catalytic results that these structural properties did not favor the hydrogenation of CO_2 to methanol. Another major reason for the low catalytic performance was that the impregnation process tended to partially block the pores in the samples (Fig. S3 and Table S2). In contrast, the Zn/t-ZrO_2 solid solution produced a new synergetic interaction by isomorphous substitution. The presence of this special solid solution caused the crystal phase diffraction peaks to shift to a higher angle and the diffraction plane spacing of the solid solution structure to decrease. In the impregnated sample, the diffraction peaks of the crystal phase shifted toward a lower angle, and the spacing of some diffraction crystal planes was increased. At the same time, the solid solution structure resulted in many oxygen vacancy defects, which promotes CO_2 activation according to some reports [30–32]. The modulation of different structural properties produced by the impregnation and solid solution methods led to two extreme structural changes and catalytic results. Compared with the physically mixed samples, the solid solution structure exhibited a high catalytic reaction efficiency, while the impregnated sample exhibited a low catalytic performance. More importantly, in the prepared solid solution samples, ZnO/t-ZrO_2-MR showed better catalytic results, and achieved a CO_2 conversion, methanol selectivity, and methanol STY of 9.2 %, 93.1 %, and 0.35 $g_{MeOH}\ h^{-1}\ g_{cat}{}^{-1}$, respectively.

From the above analysis, the excellent catalytic performance of this sample was closely related to its more uniform solid solution structure and more oxygen vacancy defects. It can thus be concluded that the large number of oxygen vacancy defects generated by the special synergetic interaction that formed in the solid solution was the primary reason for the significant improvement in the catalytic performance of such samples. However, when comparing the solid solution preparation methods, the microreaction synthesis method has incomparable technical advantages over the traditional coprecipitation method. The solid solution structure in the sample prepared by microreaction synthesis method was more uniform, resulting in more abundant oxygen vacancy defects and a superior catalytic performance for the hydrogenation of CO_2 to methanol.

It was worth mentioning that the ZnO/t-ZrO_2-MR exhibited excellent thermal stability as well from the further experimental analyses of spent samples. XRD, XPS, CO_2-TPD and H_2-TPR results of samples after 30 h on stream at 320 °C and 400 °C are shown in Fig. S6-S9 and Table 2. Compared with spent ZnO/t-ZrO_2-CP, it is obvious from XRD analysis that a larger offset degree and slope (Fig. S4) were observed in the spent ZnO/t-ZrO_2-MR. The O1s XPS spectra of spent samples are shown in Fig. 9. Combined with the O_{Sur} /(O_{Latt} + O_{Sur})data in Table 2, O_{Sur} /(O_{Latt} + O_{Sur}) in ZnO/t-ZrO_2-MR was 44 %, which was slightly lower than fresh catalyst (49 %) but significantly higher than spent ZnO/t-ZrO_2-CP sample (35 %). Similar results could be obtained from CO_2-TPD (Fig. S5) and H_2-TPR (Fig. S6) analyses. A larger CO_2 adsorption capacity and lower reduction temperatures tended to exist in spent ZnO/t-ZrO_2-MR. Interestingly, the same tendency occurred over

Table 2
XPS results of the spent ZnO/t-ZrO_2-MR and ZnO/t-ZrO_2-CP catalysts.

Catalyst	Binding energy (eV)		O_{Sur} /(O_{Latt} + O_{Sur}) (100%)
	O_{Latt}	O_{Sur}	
Spent ZnO/t-ZrO_2-MR-320 °C	529.71	531. 11	44
Spent ZnO/t-ZrO_2-CP-320 °C	529.80	531.49	35
Spent ZnO/t-ZrO_2-MR-400 °C	529.78	531. 35	42
Spent ZnO/t-ZrO_2-CP-400 °C	529.81	531. 55	33

spent samples after 30 h on stream not only at 320 °C but at higher temperature of 400 °C also. All of these results indicated that the spent ZnO/t-ZrO_2-MR still had more oxygen vacancy defects.

To test the regenerative performance of catalysts, we annealed the spent ZnO/t-ZrO_2-MR at 500 °C in air for 3 h to subtract any potential surface species. The regenerated catalyst is examined for the reaction at 320 °C and 400 °C respectively. Fig. 10 shows no noticeable decrease of catalytic performance after regeneration, which could be attributed to the retrieve of oxygen vacancy and little change in crystalline structure from the XPS shown in Fig. 11 and Table 3, and CO_2-TPD and XRD results shown in Fig. S7-S8.

4. Conclusions

Different preparation methods significantly affected the phase structure properties of Zn/Zr hybrid interfaces and the catalytic hydrogenation of CO_2 to methanol. The physical mixing method produced only two phases without the formation of any chemical interaction. The sample prepared by impregnation had a different electronic structure at the Zn/Zr interface due to the impregnation of ZnO component on the surface of mesoporous t-ZrO_2. However, ZnO component impregnation tended to block pores, and its low number of oxygen vacancy defects caused the impregnated sample to have a low catalytic efficiency. The solid solution effect increased the binding energy of the Zn/Zr interface and enhanced the interfacial interaction. The formed solid solution also produced many oxygen vacancy defects and exhibited excellent catalytic performance during CO_2 activation. More importantly, the microreaction synthesis method had incomparable technical advantages during solid solution preparation. Its unique microchannels provided an excellent mixing efficiency and high mass and heat transfers. Combined with the constant pH value in the reaction system, it provided a relatively more uniform and rapid reaction path for ZnO component. Therefore, a more uniform solid solution structure and more abundant oxygen vacancy defects were obtained, which played crucial roles in the high reaction efficiency of methanol synthesis by CO_2 hydrogenation. The catalyst obtained via microreaction synthesis exhibited excellent thermal stability and regeneration performance.

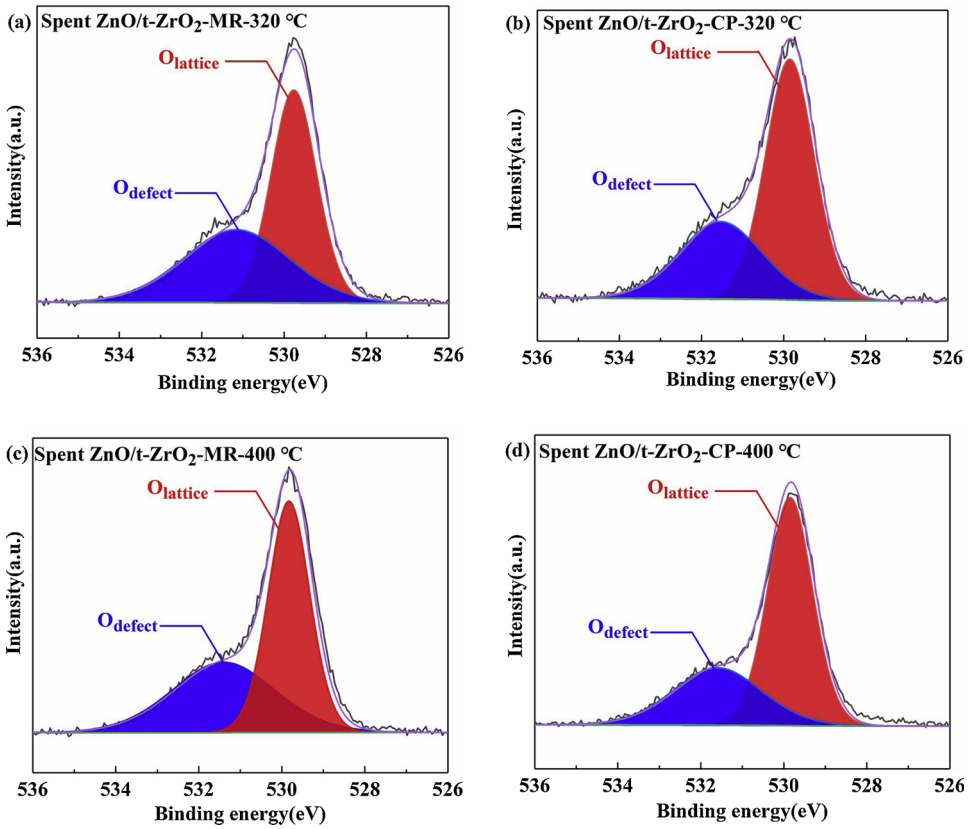

Fig. 9. XPS spectra of O1s of the (a) spent ZnO/t-ZrO_2-MR, (b) spent ZnO/t-ZrO_2-CP catalysts.

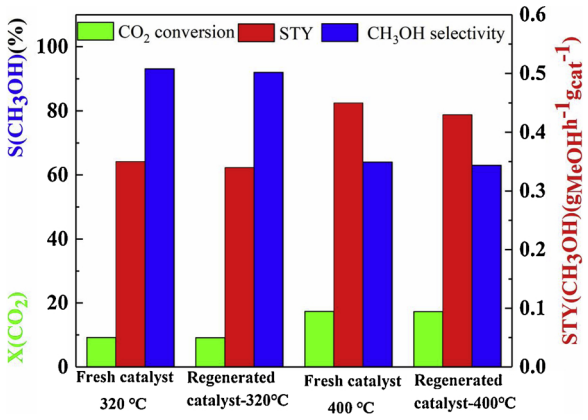

Fig. 10. Catalytic regenerative performance of ZnO/t-ZrO_2-MR.

Table 3
XPS results of the Regenerated ZnO/t-ZrO_2-MR-320 °C and ZnO/t-ZrO_2- MR-400 °C catalysts.

Catalyst	Binding energy (eV)		O_{Sur} /(O_{Latt} + O_{Sur}) (100%)
	O_{Latt}	O_{Sur}	
Regenerated ZnO/t-ZrO_2-MR-320 °C	529.84	531. 18	48
Regenerated ZnO/t-ZrO_2-MR -400 °C	529.92	531. 48	47

Declaration of Competing Interest

The authors declare that they have no known competing financial interests or personal relationships that could have appeared to influence the work reported in this paper.

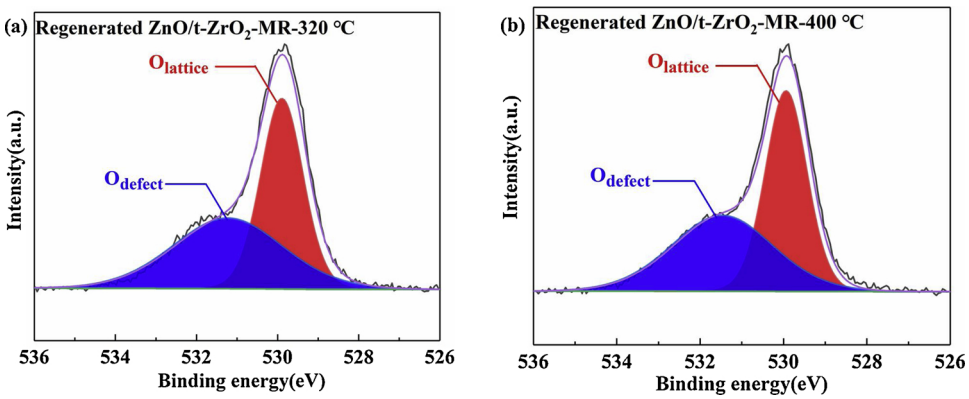

Fig. 11. XPS spectra of O1s of the (a)Regenerated ZnO/t-ZrO_2-MR-320 °C and (b) Regenerative ZnO/t-ZrO_2-MR-400 °C catalysts.

Acknowledgments

This work was supported by National Natural Science Foundation of China (NO. 21666007), Scientific and Technological Innovation Talents Team Project of Guizhou Province (NO. 20185607), One Hundred Person Project of Guizhou Province (NO. 20165655), Science and Technology Project of Guizhou Province (NO. 20175788 and 20185781), Natural Science Foundation of Guizhou Province (NO. 20177260) and Science & Technology Support Plan Project of Guizhou Provincial (No. 20182192).

Appendix A. Supplementary data

Supplementary material related to this article can be found, in the online version, at doi:https://doi.org/10.1016/j.apcata.2020.117507.

References

[1] K.P. Brooks, J. Hu, H. Zhu, R.J. Kee, Chem. Eng. Sci. 62 (2007) 1161–1170.
[2] W. Wang, S.P. Wang, Wei, et al., Chem. Soc. Rev. 40 (2011) 3703–3727.
[3] G. Glenk, S. Reichelstein, Nat. Energy 4 (2019) 216–222.
[4] J.A. Turner, Science 305 (2004) 972–974.
[5] G. Yang, N. Tsubaki, J. Shamoto, Y. Yoneyama, Y. Zhang, J. Am. Chem. Soc. 132 (2010) 8129–8136.
[6] T. Witoon, J. Chalorngtham, P. Dumrongbunditkul, M. Chareonpanich, J. Limtrakul, Chem. Eng. J. 293 (2016) 327–336.
[7] S. Kattel, P.J. Ramírez, J.G. Chen, J.A. Rodriguez, P. Liu, Science 355 (2017) 1296–1299.
[8] Y. Matsumura, J. Power Sources 238 (2013) 109–116.
[9] E.M. Fiordaliso, I. Sharafutdinov, H.W.P. Carvalho, J.D. Grunwaldt, T.W. Hansen, I. Chorkendorff, J.B. Wagner, C.D. Damsgaard, ACS Catal. 5 (2015) 5827–5836.
[10] S. Kattel, W.T. Yu, X.F. Yang, B.H. Yan, Y.Q. Huang, W.M. Wan, P. Liu, J.G.G. Chen, Angew. Chem. Int. Ed. 55 (2016) 7968–7973.
[11] J.J. Wang, G.N. Li, Z.L. Li, C.Z. Tang, Z.C. Feng, H.Y. An, H.L. Liu, T.F. Liu, C. Li, Sci. Adv. 3 (2017) e1701290.
[12] O. Martin, A.J. Martín, C. Mondelli, S. Mitchell, T.F. Segawa, R. Hauert, C. Drouilly, D. Curulla-Ferrré, J. Pérez-Ramirez, Angew. Chem. Int. Ed. 55 (2016) 6261–6265.
[13] S.S. Dang, H.Y. Yang, P. Gao, H. Wang, X.P. Li, W. Wei, Y.H. Sun, Catal. Today 330 (2019) 61–75.
[14] X.M. Liu, G.Q. Lu, Z.F. Yan, J. Beltramini, Ind. Eng. Chem. Res. 42 (2003) 6518–6530.
[15] B. Rungtaweevoranit, J. Baek, J.R. Araujo, B.S. Archanio, K.M. Choi, O.M. Yaghi, G.A. Somorjai, Nano Lett. 16 (2016) 7645–7649.
[16] J. Ye, C. Liu, D. Mei, Q. Ge, ACS Catal. 3 (2013) 1296–1306.
[17] K. Larmier, W.C. Liao, S. Tada, E. Lam, R. Verel, A. Bansode, A. Urakawa, A. Comas-Vives, C. Copéret, Angew. Chem. Int. Ed. 56 (2017) 2318–2323.
[18] N. Kumari, M.A. Haider, M. Agarwal, N. Sinha, S. Basu, J. Phys. Chem. C 120 (2016) 16626–16635.
[19] Y.X. Pan, C.J. Liu, D. Mei, Q. Ge, Langmuir 26 (2010) 5551–5558.
[20] K.H. Sun, Z.G. Fan, J.Y. Ye, J.M. Yan, Q.F. Ge, Y.N. Li, W.J. He, W.M. Yang, C.J. Liu, J. CO_2 Util. 12 (2015) 1–6.
[21] R. Grabowski, J. Słoczyński, M. Sliwa, D. Mucha, R.P. Socha, M. Lachowska, J. Skrzypek, ACS Catal. 1 (2011) 266–278.
[22] M.H. Zhang, M.B. Dou, Y.Z. Yu, Appl. Surf. Sci. 433 (2018) 780–789.
[23] M. Behrens, F. Girgsdies, Z. Anorg, Allg. Chem. 636 (2010) 919–927.
[24] J.Y. Gan, X.H. Lu, T. Zhai, Y.F. Zhao, S.L. Xie, Y.C. Mao, Y.L. Zhang, Y.Y. Yang, Y.X. Tong, J. Mater. Chem. 21 (2011) 14685–14692.
[25] H.R. Chen, J.L. Shi, T.D. Chen, J.N. Yan, D.S. Yan, Mater. Lett. 54 (2002) 200–204.
[26] V.D. Mote, Y. Purushotham, B.N. Dole, J. Theor. Appl. Phys. 6 (2012) 6.
[27] T. Kandemir, I. Kasatkin, F. Girgsdies, S. Zander, S. Kuhl, M. Tovar, R. schlogl, Top. Catal. 57 (2014) 188–206.
[28] N. Rui, Z.Y. Wang, K.H. Sun, J.Y. Ye, Q.F. Ge, C.J. Liu, Appl. Catal. B Environ. 218 (2017) 488–497.
[29] X.T. Lin, S.J. Li, H. He, Z. Wu, J.L. Wu, L.M. Chen, D.Q. Ye, M.L. Fu, Appl. Catal. B Environ. 223 (2018) 91–102.
[30] X.L. Liu, Mh. Wang, C. Zhou, W. Zhou, K. Cheng, J.C. Kang, Q.H. Zhang, W.P. Deng, Y. Wang, Chem. Commun. 54 (2018) 140–143.
[31] Z.L. Li, J.J. Wang, Y.Z. Qu, H.L. Liu, C.Z. Tang, S. Miao, Z.C. Feng, H.Y. An, C. Li, ACS Catal. 7 (2017) 8544–8548.
[32] P. Gao, S.S. Dang, S.G. Li, X.N. Bu, Z.Y. Liu, Z.Y. Liu, M.H. Qiu, C.G. Yang, H. Wang, L.S. Zhong, Y. Han, Q. Liu, W. Wei, Y.H. Sun, ACS Catal. 8 (2018) 571–578.